



HAL
open science

Initial investigation of B₄C–TiB₂ composites as neutron absorption material for nuclear reactors

J. Wang, D. Ren, L Chen, G Man, H. Zhang, L. Luo, W. Li, Y.B. Pan, P Gao, Y. Zhu, et al.

► To cite this version:

J. Wang, D. Ren, L Chen, G Man, H. Zhang, et al.. Initial investigation of B₄C–TiB₂ composites as neutron absorption material for nuclear reactors. *Journal of Nuclear Materials*, 2020, 539, pp.152275. 10.1016/j.jnucmat.2020.152275 . hal-02931972

HAL Id: hal-02931972

<https://hal.science/hal-02931972v1>

Submitted on 10 Sep 2020

HAL is a multi-disciplinary open access archive for the deposit and dissemination of scientific research documents, whether they are published or not. The documents may come from teaching and research institutions in France or abroad, or from public or private research centers.

L'archive ouverte pluridisciplinaire **HAL**, est destinée au dépôt et à la diffusion de documents scientifiques de niveau recherche, publiés ou non, émanant des établissements d'enseignement et de recherche français ou étrangers, des laboratoires publics ou privés.

Ji Wang: Conceptualization, Methodology, Investigation, Writing – original draft, Writing - review & editing, Visualization. **Donglou Ren:** Methodology, Investigation, Writing – original draft, Writing - review & editing, Visualization. **LeiLei Chen:** Investigation, resources. **Guian Man:** Writing - review & editing, software. **Houyuan Zhang:** Writing - review & editing, software. **Hongpeng Zhang:** Investigation, resources. **Laihui Luo:** Conceptualization. **Weiping Li:** Conceptualization. **Yanbo Pan:** Resources. **Peifeng Gao:** Conceptualization, Methodology, Writing - review & editing, software, Funding acquisition, Supervision. **Yabin Zhu:** Conceptualization, Methodology, Writing - review & editing, resources, Supervision. **Zhiguang Wang:** Conceptualization, Methodology, Supervision, Funding acquisition.

23 Abstract

24 In this study, a specifically designed B_4C-TiB_2 composite with the
25 typical microstructural feature of a TiB_2 network (cages) that
26 encapsulates a B_4C matrix was fabricated by the molten-salt and spark
27 plasma sintering (SPS) method. The finite-element (FE) calculation
28 results show that the connected TiB_2 cages constitute a thermally
29 conductive network, which effectively improves the overall thermal
30 conductivity of the composite; these results agree well with the
31 experimental results. Moreover, the Vickers indentation results reveal that
32 the TiB_2 network (cages) can effectively impinge/block the propagation
33 of cracks, which increases the composite toughness. The composite was
34 subjected to helium (He) ion irradiation to simulate the situation in which
35 the B_4C-TiB_2 composites serve as neutron absorption material, and for
36 which case a high quantity of He atoms is produced by the $B^{10}(n, \alpha) Li^7$
37 nuclear reaction. According to the transmission electron microscopy
38 (TEM) results, the interfaces between TiB_2 and B_4C act as effective sinks
39 for He atoms, and are preferential nucleation sites for He bubbles. The
40 theoretical and experimental results show that when the B_4C-TiB_2
41 composites serve as neutron absorption pellets in nuclear reactors, they
42 exhibit a better resistance to their disintegration than pure B_4C pellets.
43 Consequently, the performance of the control rods of nuclear reactors can
44 be improved.

45 Keywords: neutron absorber; B₄C pellet; He irradiation; crack
46 propagation; finite element.

47

Journal Pre-proof

48 1. Introduction

49 B_4C is widely used as a neutron absorption material for control rods
50 (CRs) in many nuclear reactor systems, in particular in fast reactor
51 systems [1] (e.g., Phenix (France), BN (Russia), JOYO (Japan), ALMR,
52 FFTF (United States)) owing to its high melting temperature, outstanding
53 thermal stability, good mechanical properties, and the high neutron
54 absorption cross section of ^{10}B ; B_4C neutron absorbers play an important
55 role regarding the performance of CRs by, for example, adjusting the
56 reactivity compensation during the normal operation cycles of nuclear
57 reactors, initiating/terminating an operation cycle for refueling or reactor
58 component maintenance, and rapidly shutting down the reactor if
59 abnormal conditions occur. Therefore, B_4C neutron absorbers are of
60 primary importance for the safe and efficient operation of nuclear
61 reactors.

62 In many CR designs (e.g., JOYO), B_4C materials are usually
63 presented in the form of pellets. However, during the operation lifetime of
64 CRs, B_4C pellets often fracture into pieces and even powders [2]. These
65 fractured B_4C pellet pieces progressively fill the gaps between the pellets
66 and cladding materials, which accelerates the absorber-cladding
67 mechanical interaction [2]. This leads to an incompatibility between the
68 cladding materials and other components of reactors (e.g., induced
69 absorber swelling cladding cracking (IASCC)) and shortens the CR

70 lifetime. Moreover, the cracked materials are very sensitive to the
71 subsequent radiation-assisted dissolution (i.e., radiolysis effects [3-5]).
72 Regarding water-cooled nuclear systems, when cooling water leaks into
73 the pellet capsule owing to IASCC-induced cracking [6], the radiolysis
74 effect accelerates the dissolution of the absorber materials and promotes
75 the disintegration of B_4C pellets [5]. Both effects degrade the CRs and
76 safe operation of nuclear reactors.

77 According to previous research studies, the disintegration of bulk
78 B_4C ceramic pellets is closely associated with the
79 thermal-gradient-induced macrocracks and swelling-gradient-induced
80 microcracks [7]. During the service lifetime of CRs, the (n, α) nuclear
81 reaction releases an average energy of 2.78 MeV per event [1]; the most
82 energy is deposited within the B_4C matrix. For instance, at a CR burnup
83 of 10^{22} cap/cm³ per year, a volume power of 1.5×10^2 W/cm³ is deposited
84 in the B_4C pellets. Owing to the low thermal conductivity of B_4C and the
85 high heat-generation rate caused by the $^{10}B (n, \alpha) ^7Li$ reaction, the
86 temperature gradient of B_4C pellets can reach up to 10^3 K/cm. Such a high
87 temperature gradient causes a great thermal stress and results in
88 thermal-stress-induced macrocracks. Moreover, a high quantity of He
89 atoms produced by the transmutation reaction accumulate in the form of
90 flat lenticular He bubbles [8,9]. These He bubbles cause significant
91 volume swelling. When the neutron absorption pellets are placed in

92 thermal neutron reactors, owing to the self-shielding effect [7,10], the
93 burnup of the pellet periphery is usually stronger than that of the interior.
94 Because the He atom production is proportional to the burnup level, a
95 gradient distribution of He bubbles leads to a steep swelling gradient of
96 the B_4C material and an abrupt local strain [7]: the consequence are
97 swelling-gradient-induced microcracks. In general, the released heat and
98 He atoms produced by the $^{10}B(n, \alpha)^7Li$ reaction are two factors that lead
99 to the formation of cracks. Both factors promote the formation of
100 macro-scale cracks and facilitate the crack propagation through pellets,
101 which result in their disintegration [2,11].

102 Therefore, it is of vital importance to improve the thermal
103 conductivity and irradiation-induced swelling resistance of B_4C absorber
104 materials to guarantee the good long-term performance of CRs and a safe
105 and efficient operation of nuclear reactors. B_4C -diborides composites
106 have been explored a long time ago to improve the performance of B_4C in
107 the irradiation field. For example, B_4C - HfB_2 composite was designed to
108 improve fracture toughness [12, 13] and the thermal-mechanical
109 properties of the neutron absorber [12]. In this study, a low economic cost
110 and honeycomb-structured B_4C - TiB_2 composite was elaborated to attain
111 the aforementioned objective. The main feature of the composite is a
112 highly thermally conductive cage-like TiB_2 network that encapsulates
113 conventional B_4C matrix grains. TiB_2 has a high melting point (3498 K),

114 exceptional hardness (25-35 GPa), highly thermal conductivity, excellent
115 wear resistance, a low thermal expansion coefficient ($4.6 \times 10^{-6} \text{ K}^{-1}$,
116 which is almost the same as that of B_4C , $4.5 \times 10^{-6} \text{ K}^{-1}$), and a high
117 oxidation resistance [14-18]. Owing to the inimitable characteristics of
118 TiB_2 , it is therefore selected as the cage-like structure of the $\text{B}_4\text{C-TiB}_2$
119 composites. The good features of conventional B_4C material are
120 maintained, and the thermal conductivity of the composite is significantly
121 improved with respect to that of the pure B_4C material. In addition, the
122 composite exhibits many interfaces.

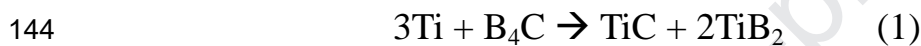
123 The $\text{B}_4\text{C-TiB}_2$ composites were subjected to He ion irradiation to
124 simulate the situation in which the $\text{B}_4\text{C-TiB}_2$ composite is exposed to a
125 high neutron flux, and a high quantity of He atoms is produced by the (n,
126 α) reaction. Moreover, a series of post-irradiation analyses and FE
127 calculations were conducted to evaluate the behavior of the $\text{B}_4\text{C-TiB}_2$
128 component in a nuclear reactor environment.

129 2. Experimental details

130 2.1. Material synthesis

131 A two-step synthesis method was employed to synthesize the $\text{B}_4\text{C-}$
132 TiB_2 composite [19]. In the first step, Ti and B_4C powders were mixed
133 with NaCl and KCl in an Al_2O_3 crucible. The mixtures with initial $\text{B}_4\text{C/Ti}$
134 molar ratios of 6:1, 4:1, and 2:1 were exposed to an Ar atmosphere at
135 1273 K. After the (1) and (2) in-situ reactions in the melted salt bath, a

136 uniform TiB_2 coating occurred on the B_4C particles. The remnant NaCl,
137 KCl, and other impurities were washed away with deionized water, and
138 the samples were subsequently dried to obtain dry TiB_2 -coated B_4C
139 powders. Note that the melt point of NaCl and KCl mixing is low (~ 933
140 K) and the liquid mass transfer mode between B_4C and Ti in the molten
141 salts guarantees the uniform nucleation and growth of TiB_2 on the surface
142 of B_4C particles. Therefore, the NaCl and KCl were employed as the
143 medium for reactions.



146 In the second step, the mixtures containing uniformly TiB_2 -coated B_4C
147 powders with different TiB_2 contents were sintered in a spark plasma
148 sintering (SPS) system (SPS-20T-15, Chen Hua) with the same procedure
149 to obtain three cylindrical bulk samples with diameters of 13 mm and
150 heights of 2 mm (denoted as S1, S2, and S3). In the SPS procedure, the
151 heating rates are 50 K/min from RT to 1673 K, and 25 K/min from 1673
152 K to 1973 K, respectively. The holding time and temperature are 10 min
153 and 1973 K, respectively. The pressure during the holding stage is 45
154 MPa. The cooling rate is 50 K/min from the holding temperature to RT.
155 Each bulk sample has a relative density of 100%. The volume fractions of
156 TiB_2 phases in B_4C - TiB_2 composites are determined by the equation (3).

$$157 \quad \frac{V_{TiB_2}}{V_t} = \frac{\frac{m_{TiB_2}}{\rho_{TiB_2}}}{\frac{m_t}{\rho_t}} = w_{TiB_2} \cdot \frac{\rho_t}{\rho_{TiB_2}} \quad (3)$$

158 Where V_{TiB_2} and V_t are the volume of TiB_2 phases and the B_4C-TiB_2
 159 composites, respectively. w_{TiB_2} is the weight percent of TiB_2 measured
 160 by using XRD, the calculated weight percent of TiB_2 for S1, S2 and S3
 161 are 18 %, 26% and 44%, respectively. ρ_{TiB_2} (4.5 g/cm^3) is the density of
 162 TiB_2 and ρ_t is the density of the B_4C-TiB_2 composites (2.637, 2.796 and
 163 3.051 g/cm^3 for S1, S2 and S3, respectively). The density of the B_4C-TiB_2
 164 composites were measured by and Archimedes method. The chemical
 165 composition and the calculated volume fraction of each sample are shown
 166 in Table 1.

167 2.2. Vickers indentation tests and irradiation procedure

168 A pyramidal diamond tip with an apical angle of 136° was used to
 169 perform Vickers indentation tests. The tests were performed on the
 170 surface of the virgin samples to investigate the crack propagation
 171 behavior in the composite. During the indentation tests, the maximal load
 172 was set to 9.8 N, and the holding time was 15 s. Each indentation was set
 173 more than $100 \mu\text{m}$ apart to avoid an overlap of the indentation-induced
 174 deformations or crack outspread regions.

175 The He ion irradiation procedure was conducted in a terminal
 176 chamber with a 320 kV multidiscipline research platform for highly

177 charged ions at the Institute of Modern Physics (IMP), Lanzhou, China.
178 Samples S1, S2, and S3 were irradiated with 500 keV He ions with
179 1×10^{17} ions/cm² at 773 K. After the irradiation process, the samples were
180 annealed at 1273 K for 25 min in a vacuum of 10^{-5} Pa. In addition,
181 Stopping Range of Ions in Matter (SRIM) codes were conducted with the
182 Kinchin–Pease quick-calculation mode to predict the distribution of the
183 He atoms and displacement damage in B₄C and TiB₂, respectively. The
184 calculated distribution is a function of the penetration depth, as shown in
185 Fig. 1; the Bragg peak with a He concentration of 8.92×10^{21} cm⁻³ (7.02%)
186 is located at a depth of ~ 1.38 μ m in the B₄C material, and 7.18×10^{21}
187 cm⁻³ (6.14%) at a depth of ~ 1.56 μ m in TiB₂ material, respectively.

188 2.3. Characterization

189 The morphology of the sample surface and Vickers indentation
190 impression were recorded by scanning electron microscopy (SEM,
191 Thermo Fisher Quanta FEG 250). In addition, the focused ion beam
192 technology (Thermo Fisher, Helios G4 CX) was employed to lift up thin
193 foils for the transmission electron microscopy (TEM) analysis. The thin
194 foils were analyzed with a Talos F200X TEM at 200 kV in the
195 bright-field mode, and a HV-1000 indentation test machine (Shanghai
196 Lianer Testing Equipment Corporation) was used to perform the Vickers
197 indentation tests.

198 3. Results and discussions

199 Before the SEM analysis, the composites were mechanically
200 polished with diamond papers (from 800 to 12500 grit) until mirror-like
201 surfaces were obtained. Fig. 2 shows the typical SEM images of the B₄C–
202 TiB₂ composites with TiB₂ volume fractions of 10.5% (Fig. 2(a)), 16.2%
203 (Fig. 2(b)), and 29.8% (Fig. 2(c)). The white contrast indicated by black
204 arrows in the SEM images are TiB₂ phases, and the left, dark contrast
205 represents B₄C grains. The TiB₂ phases are distributed along the B₄C
206 grain boundaries. With increasing TiB₂ phase volume fraction, the
207 fraction of isolated TiB₂ particles decreases, and more and more TiB₂
208 phases along the grain boundaries become connected, which results in an
209 interconnected network from the two-dimensional (2D) point of view
210 (Fig. 2(c)). Therefore, from the three-dimensional point of view, the TiB₂
211 network forms a cage-like structure, which encapsulates the B₄C matrix
212 grains. The average thickness of the TiB₂ network of S3 is 0.9 μm, and
213 the statistical measurement based on the line-intercept method [20]
214 reveals that the mean grain sizes of B₄C in the S1, S2, and S3 samples are
215 9.5, 8.6, and 6.4 μm, respectively. Thus, the TiB₂ fraction increases at the
216 expense of consumed B₄C.

217 To evaluate the effect of the TiB₂ network (cages) and its volume
218 fraction on the heat transfer performance in the B₄C–TiB₂ composites, a
219 series of numerical studies based on the typical microstructures of pure
220 B₄C and B₄C–TiB₂ composites were implemented in the FE program

221 ABAQUS. The geometric constructions of the 2D pure B_4C and B_4C -
222 TiB_2 composites FE model is shown in Fig. 3. A thermal continuity
223 constraint was defined at each interface to connect the B_4C and TiB_2
224 domains without heat dissipation. An initial temperature of 773 K was
225 assigned to the entire computational region to simulate the reactor
226 environment temperature, and 1273 K (boundary condition) was assigned
227 to the left end of each model to generate a stable heater source; the other
228 boundary conditions were adiabatic boundary conditions. The
229 temperature dependence of the physical parameters of B_4C and TiB_2 used
230 in the numerical calculation are listed in Table 2 [18,21].

231 The temperature distributions used with different time scales for the
232 pure B_4C and B_4C - TiB_2 composites models are shown in Fig. 4. The
233 temperature distribution in pure B_4C is homogeneous along the vertical
234 direction, and the isotherms are perpendicular to the horizontal axis.
235 Whereas the temperature in the B_4C - TiB_2 composites presents an
236 irregular gradient distribution. Furthermore, the temperature gradient in
237 the B_4C - TiB_2 composites with a high TiB_2 volume fraction is lower than
238 that of the low TiB_2 volume fraction. Particularly, the maximum
239 temperature gradient appears in pure B_4C . Thus, heat is transmitted faster
240 in the B_4C - TiB_2 composite than in the pure B_4C , the higher the volume
241 fraction of TiB_2 , the faster the heat transfers, which is consistent with the
242 experimental results in [19].

243 To compare the heat transfer performance of the four structures
244 quantitatively, the temperature variations at the middle point of the
245 right-end boundary in each model are presented with respect to time in
246 Fig. 5. The heating rate in the B_4C - TiB_2 composite with higher TiB_2
247 volume fraction is higher than that of lower ones. For example, the
248 temperature at point P_3 in the B_4C - TiB_2 composite with the highest TiB_2
249 volume fraction (29.8%) reaches 1181 K within 1 μs , while the
250 temperature at point P_0 in the pure B_4C becomes only 1076 K within the
251 same time. The FE analysis results demonstrate that the lower
252 temperature gradient caused by the faster heat propagation in the B_4C -
253 TiB_2 composites can be ascribed to the existence of the TiB_2 network in
254 the B_4C matrix, which has a higher thermal conductivity. If the
255 composites are used as neutron-absorbing pellets in nuclear reactors, their
256 high thermal conductance can rapidly cool the local high temperature
257 caused by the nuclear reactions and greatly reduce the thermal stress
258 caused by the thermal gradient, which reduces the risk of structural
259 failure.

260 To further determine the equivalent average parameters and average
261 heat conducting characteristics of the B_4C - TiB_2 composite, the equivalent
262 homogeneous models with all the homogenized model parameters, such
263 as conductivity, specific heat and density, determined by the
264 volume-weighted-average were implemented for the three cases of

265 different TiB_2 volume fractions (10.5%, 16.2% and 29.8%). Taking the
266 temperature of the middle point of the right-end boundary as the
267 assessment during simulation from 0.2 to 1 μs , the comparison of the
268 results calculated from real composite structure and equivalent
269 homogeneous models are summarized in Table 3. It can be seen that the
270 results of the equivalent homogeneous models are slightly overestimated
271 for the three cases, but the maximum relative error is less than 5%, which
272 indicates that the simple volume-weighted-average method can be used to
273 roughly predict the equivalent parameters and average heat conducting
274 characteristics of the B_4C - TiB_2 composite for variational volume fraction.
275 It demonstrates the expected conductivity enhancement brought by the
276 interconnectivity of the TiB_2 phases as well.

277 In real nuclear reactors, the thermal gradient and He
278 swelling-induced crack propagation in B_4C materials are mainly
279 responsible for the disintegration of B_4C pellets in fast neutron reactors
280 and in thermal neutron reactors, respectively. To investigate the effect of
281 the TiB_2 network (cages) on the crack propagation behavior in the B_4C -
282 TiB_2 composites, Vickers indentation was employed to simulate the
283 external stress that was applied to the B_4C - TiB_2 composites.

284 The typical Vickers indentation marks on the surfaces of S1, S2, and
285 S3 are shown in Figs. 6(a), (b), and (c), respectively. The beginnings and
286 endings of the cracks are indicated by double-headed arrows. Note that in

287 the Fig. 6(c), the gradient of sunken area is steep, outline of the Vickers
288 indentation impression is irregular, but four cracks of the indentation are
289 obvious. Therefore, each crack length is measured from the end of the
290 crack, and along the inverse direction of crack propagation to the point
291 where crack origins from the steeply sunken area (i.e. the indentation
292 impression area). At a load of 9.8 N, the length of the cracks on S1 range
293 from 20.7 to 27.9 μm ; those on S2 and S3 range from 12.8 to 20.3 μm
294 and 6.8 to 13.5 μm , respectively. The statistical results of the cracks show
295 that the average values are 22.9 ± 2.8 , 16.1 ± 4.3 , and 12.2 ± 3.8 μm for
296 S1, S2, and S3, respectively. Fig. 7 presents the statistical results of the
297 crack lengths on S1, S2, and S3, respectively. Evidently, the crack lengths
298 decrease with increasing TiB_2 volume fraction. Thereby the statistical
299 results prove that the TiB_2 phase distribution along the grain boundaries
300 can impinge/block the crack propagation.

301 Figs. 8(a) and (b) present the enlarged SEM images of the crack
302 propagation paths in S1 and S3, respectively. The white contrast in Figs.
303 8(a) and (b) are TiB_2 phases: the TiB_2 phases in Fig. 8(a) are isolated
304 particles, which are distributed in the B_4C matrix; the TiB_2 phases in Fig.
305 8(b) are interconnected, thereby forming a network (cages). The solid
306 arrow in Fig. 8(a) indicates clearly that the propagating crack departs
307 from its original straight trajectory and curves along the $\text{B}_4\text{C}/\text{TiB}_2$
308 interface, thereby proving that the isolated TiB_2 islands in the B_4C matrix

309 can redirect the crack propagation. A similar phenomenon was reported in
310 [22]. In this study, the network (cages) topography in Fig. 8(b) clearly
311 shows that the crack propagates through the TiB_2 walls (dashed arrows 2
312 and 3) and extends along the interface between the B_4C and TiB_2 phases
313 (dashed arrow 1), which facilitates the energy release of the crack tip.
314 This is confirmed by the shorter crack length ($12.2 \pm 3.8 \mu\text{m}$) of S3 than
315 those of S1 ($22.9 \pm 2.8 \mu\text{m}$) and S2 ($16.1 \pm 4.3 \mu\text{m}$), as shown in Fig. 6.

316 It can be concluded that there are two underlying ways in which the
317 TiB_2 phases affect the crack propagation in B_4C - TiB_2 composites: first,
318 when the volume fraction of the TiB_2 phase is low, TiB_2 distributes in the
319 B_4C matrix as isolated particles (shown in Fig. 8(a)), and when the
320 propagation of a crack tip encounters a TiB_2 particle, the crack moves
321 along the $\text{B}_4\text{C}/\text{TiB}_2$ interface, prolongs the crack propagation length and
322 dissipates more energy, finally results in an improvement of the fracture
323 toughness of the B_4C - TiB_2 composites. Similar dissipation mechanisms
324 at the $\text{B}_4\text{C}/\text{TiB}_2$ interfaces are also found in Refs. [23, 24]. Second, when
325 the volume fraction of the TiB_2 phase is high, the TiB_2 phase forms an
326 enclosed cage-like structure that encapsulates the B_4C grains (Fig. 8(b)).
327 Thus, the cracks have to penetrate the TiB_2 walls before extending along
328 the $\text{B}_4\text{C}/\text{TiB}_2$ interfaces or must propagate through the neighboring B_4C
329 grains. According to the model of Cook et al. on crack propagation in
330 brittle systems [25], additional energy is required to deflect the crack

331 propagation and initiate secondary crack propagation across the interface;
332 the primary crack requires much energy.

333 To quantitatively measure the fracture toughness of the B₄C-TiB₂
334 composites, following equations are used [26]:

$$335 \quad K_{IC} = 0.016(E/H_V)^{0.5} P c^{-1.5}, \quad (4)$$

336 where

$$337 \quad H_V = \frac{1.8544 \times P}{4a^2 \times 1000}, \quad (5)$$

338 in which E is the Young's modulus, H_V the Vickers hardness, P the
339 Vickers indentation load, and a and c are the half length of the residual
340 Vickers indenter impression diagonal and half length of the radial crack
341 diagonal, respectively. The fracture toughness of the composites K_{IC}
342 were calculated to be 3.06 ± 0.28 (MPa·m^{1/2}), 3.81 ± 0.33 (MPa·m^{1/2}), and
343 4.38 ± 0.67 (MPa·m^{1/2}) for S1, S2, and S3, respectively. In other words,
344 increasing the TiB₂ volume fraction and optimizing the distribution of
345 TiB₂ can impinge/block the propagation of cracks and improve the
346 fracture toughness of the B₄C-TiB₂ composites. This promotes the
347 integration of B₄C pellets and improves the CR performance in the harsh
348 environments of nuclear reactors.

349 He behavior of the composites under irradiation conditions is
350 important for the evaluation of the composites serving in the reactors,
351 however, it was seldomly studied. Therefore, we conducted He ions
352 irradiation on the composites and initially investigated the He behavior by

353 TEM observation.

354 The TEM images in Fig. 9 show the He bubble distribution and
355 morphology in B₄C phase of samples S1, S2, and S3. The images were
356 recorded with the same underfocus of 2.8 μm. The He bubbles, which are
357 small bright dots in the images, are located within a band area. The width
358 of He bubbles deposition band is smaller than that of the implanted band
359 as calculated by SRIM, similar phenomenon is observed by Motte et al.
360 [8]. It is suggested that this is due to the different depths of the He ions
361 induced damage profile and the He ions implanted profile. In the area of
362 the damage profile, lot of vacancies were introduced by energetic ions
363 collision, while in the area of He atoms implanted band, He atoms greatly
364 outnumbered the vacancies. In the overlapped areas (the width of which
365 was smaller than the implanted band as calculated by SRIM), abundant
366 vacancies and He atoms promoted the formation of He-vacancy clusters
367 and increased the density of He bubble germs. After annealing,
368 He-vacancy clusters evolved into visible He bubbles under TEM
369 observation and formed a bubbles band in the overlapped area. Moreover,
370 Gillet et al. found that the dissociation energy of He-vacancy is ~ 2 eV,
371 the high energy barrier inhibited the He diffusion by the formation of
372 He-vacancy clusters [27], and this explained that no He bubbles outside
373 the band area can be found (excepted the He bubbles in the grain
374 boundaries).

375 The He bubbles in the bubbles band are small and dense; such
376 feature has been argued to arise partially from the diffusion behavior of
377 He atoms in B_4C . According to Refs. [27-30], He atoms must overcome a
378 high energy barrier to migrate even through the most probable migration
379 paths owing to the intrinsic chemical bond and lattice structure of B_4C .
380 Schneider et al. discovered that He atoms prefer to migrate between $\langle 111 \rangle$
381 planes by first-principle calculations. Moreover, they discovered that the
382 activation energy of He ion diffusion is approximately 2 eV [28], which is
383 consistent with the experimental results in [30]. The 2 eV migration
384 energy means that the aggregation of He atoms in B_4C materials is
385 retarded and explains the observation of small-sized He bubbles in this
386 study rather than large-sized He bubbles in metals under similar
387 irradiation conditions [31].

388 The He bubbles that are distributed along the interfaces are bigger
389 than the bubbles distributed in the B_4C and TiB_2 grains (however, bubbles
390 along the TiB_2 - TiB_2 interface are not investigated in this study), as shown
391 in Fig. 10. This is due to the special structure of the interface. Misfits in
392 the lattice structure of the interfaces contain plenty of open volume [32],
393 which provides adequate free space for the deposition of
394 irradiation-induced point defects (e.g., vacancies, interstitials, transmuted
395 elemental atoms) [33]. Owing to the high binding energy between
396 vacancies and He atoms (~ 2 eV [27,28]), the open volume of interfaces

397 can act as efficient trapping sites for He and preferential nucleation sites
398 for He bubbles [8,9,34]. Therefore, once the He atoms are captured by the
399 interfaces, they cannot easily be released within the temperature range
400 investigated in this study. As shown in Fig. 10, no He bubbles depleted
401 zone was detected, which is consistent with the results of Motte et al.'s
402 work [28] that it was hard for He atoms to diffuse through or in the B₄C
403 grain boundaries below 1373 K. This might prove that long-range He
404 diffusion is negligible at 1273 K. Moreover, TEM image in Fig. 10 shows
405 that He bubbles deposition band in B₄C is closer to the surface than that
406 in TiB₂, this phenomenon is also consistent with SRIM calculation as
407 shown in Fig. 1 that the overlap of He distribution and damage profile is
408 shallower in B₄C than that in TiB₂.

409 In a realistic environment of nuclear reactors, increasing the density
410 of sinks for the precipitation of He atoms is an effective way to suppress
411 the formation of large He bubbles [35], and reduce the He-induced
412 property degradation (e.g. He embrittlement). Therefore, the network
413 (cages) of the TiB₂ phases provides numerous sinks for He precipitation,
414 which might inhibit the formation of large He bubbles, and mitigate the
415 effects of He-accumulation-induced shear stress at interfaces, and the
416 resulting microcracks, especially in the thermal neutron reactors.
417 However, other factors may affect performance of the B₄C–TiB₂
418 composites, such as shear stress induced by He accumulation at the

419 interfaces, different thermal dilation between B_4C and TiB_2 . To have a
420 better evaluation of the B_4C - TiB_2 composites in a realistic environment, a
421 detailed numerical evaluation will be carried out in the future study.

422 As an important component of the B_4C -diborides composites, the
423 behavior of diborides under irradiation environment is very crucial to the
424 performance of composites. Cheminant et al. conducted neutron
425 irradiation on HfB_2 , and found that porosity appeared at grain boundaries,
426 and resulted in a decrease of the thermal diffusivity [36], which lead to
427 the degradation of B_4C - HfB_2 composites. Regarding the TiB_2 in this
428 study, despite the inimitable merits of TiB_2 , however, its irradiation
429 behavior was seldomly studied, which is very important for the
430 application of TiB_2 as neutron absorbers. To the best of our knowledge,
431 only two studies reported the microstructural evolution of TiB_2 under
432 irradiation conditions [37, 38]. Therefore, a systematic study on the
433 irradiation tolerance of TiB_2 is needed, which will be part of our future
434 work.

435 3. Conclusion

436 To improve the performance of B_4C neutron absorption material in
437 nuclear reactors, a set of property-optimized B_4C - TiB_2 composites were
438 designed and fabricated through a combination of the molten-salt and
439 SPS methods. The TiB_2 phase distributes along the B_4C grain boundaries
440 and forms a connected network (cages), which encapsulates the B_4C

441 matrix phase. The thermal conductivity and fracture toughness of the
442 B_4C-TiB_2 composites are greatly improved owing to the special cage-like
443 structure. The FE analyses show that the connected TiB_2 network
444 promotes the heat transfer and improves effectively the overall thermal
445 conductivity of the B_4C-TiB_2 composite. The improved thermal
446 conductivity results in a lower thermal stress, which mitigates
447 thermal-stress-induced crack propagation.

448 Vickers indentation tests were performed on the composites to study
449 the crack propagation behavior. The TiB_2 network (cages) can effectively
450 impinge/block the crack propagation, thereby improving the composite
451 fracture toughness. This is important for maintaining the integration of
452 B_4C-TiB_2 composites if the composite serves as neutron absorption
453 material in nuclear reactors.

454 Moreover, He ion irradiation was used to investigate the He behavior
455 in the composites and to simulate the situation in which a high quantity of
456 He is produced by the $B^{10}(n, \alpha) Li^7$ nuclear reaction. The TEM results
457 show that the interfaces of B_4C and TiB_2 are effective trapping sites for
458 He atoms and nucleation sites for He bubbles. Note that in a fast neutron
459 reactor, the ballistic damage induced by energetic neutrons scattering and
460 the nuclear reaction products (e.g., He, Li) scattering are much higher
461 than the sole He ions implantation, this leads to a higher vacancy/He ratio
462 and the possible consequences on the defects dynamics [28].

463 Overall, this study provides a synthesis method for fabricating
464 neutron absorption materials for the application in nuclear reactors. The
465 special property-optimized B_4C-TiB_2 composites with designed
466 microstructure exhibit a better resistance to disintegration under
467 irradiation and in the thermodynamic environment of nuclear reactors. In
468 addition, they have a great potential for the application as
469 neutron-absorbing pellets in nuclear reactors.

470 In the future study, other issues will be addressed to have a
471 comprehensive evaluation of B_4C-TiB_2 composites under irradiation
472 conditions. For example, helium behavior in TiB_2 and irradiation
473 resistant property of TiB_2 , effects of the special cage-like structure and
474 TiB_2 content on He diffusion and release during annealing, other
475 synthesis routes to optimize the structure and properties of the B_4C-TiB_2
476 composites, influence of He bubbles aggregation along the B_4C-TiB_2
477 and TiB_2-TiB_2 interface on the thermal conductivity of the composites
478 and the crack propagation behavior, etc.

479 Acknowledgements

480 This research was supported by the National Natural Science
481 Foundation of China (No. 11902129, 11805245), Strategic Priority
482 Research Program of Chinese Academy of Sciences (No. XDA21010202),
483 Natural Science Fund of Zhejiang Province (No. LQ20A050001), Natural
484 Science Fund of Ningbo City (No. 2019A610183), and China

485 Postdoctoral Science Foundation (2019T120963).

486 Data availability

487 The raw data required to reproduce these findings cannot be shared at
488 this time as the data is part of an ongoing study. The processed data
489 required to reproduce these findings cannot be shared at this time as the
490 data is part of an ongoing study.

491 References

492 [1] T. Donomae, K. Maeda, Fast Spectrum Control Rod Materials, in:
493 R.J.M. Konings, T.R. Allen, R.E. Stoller, S. Yamanaka (Eds.),
494 Comprehensive nuclear materials, Elsevier, Netherlands, 2012, pp.
495 509-534.

496 [2] T. Maruyama, S. Onose, T. Kaito, H. Horiuchi, J. Nucl. Sci. Technol.
497 34 (10) (1997) 1006-1014.

498 [3] N. Moncoffre, N. Toulhoat, N. Bererd, Y. Pipon, G. Silbermann, A.
499 Blondel, N. Galy, P. Sainsot, J.-N. Rouzaud, D. Deldicque, V. Dauvois, J.
500 Nucl. Mater. 472 (2016) 252-258.

501 [4] V. Kerleguer, C. Jegou, L. D. Windt, V. Broudic, G. Jouan, S. Miro, F.
502 Tocino, C. Martin, J. Nucl. Mater. 529 (2020) 151920.

503 [5] D. Gosset, Absorber materials for generation IV reactors, in: P. Yvon,
504 Structural Material for Generation IV Nuclear reactors, Elsevier,
505 Netherlands, 2017, pp. 533-567.

506 [6] IAEA-TECDOC-1132, Control Assembly Materials for Water

- 507 Reactors: Experience, Performance and Perspectives, 1998.
- 508 [7] G.W. Hollenberg, J.A. Basmajian, *J. Am. Ceram. Soc.* 65 (4) (1982)
- 509 179-181.
- 510 [8] V. Motte, D. Gosset, G. Gutierrez, S. Doriot, N. Moncoffre, *J. Nucl.*
- 511 *Mater.* 514 (2019) 334-347.
- 512 [9] T. Stoto, J. Ardonceau, L. Zuppiroli, M. Castiglioni, B. Weckermann,
- 513 *Radiat. Eff.*, 105 (1987) 17-30.
- 514 [10] R. M. Horn, B. D. Frew, P. V. Diemen, Thermal Spectrum Control
- 515 Rod Materials, in: R.J.M. Konings, T.R. Allen, R.E. Stoller, S. Yamanaka
- 516 (Eds.), *Comprehensive nuclear materials*, Elsevier, Netherlands, 2012, pp.
- 517 485-507.
- 518 [11] D. Gosset, M. Colin, *Tech. Ing.* BN3720 (2007).
- 519 [12] G.M. Decroix, D. Gosset, B. Kryger, M. Boussuge, H. Burlet,
- 520 Improvement of thermomechanical properties of ceramic materials for
- 521 nuclear applications, in: P. Vincenzini (Ed.), 8th CIMTEC, Florence, Italy,
- 522 1994.
- 523 [13] K. Sairam, J.K. Sonber, T.S.R.Ch. Murthy, C. Subramanian, R.C.
- 524 Hubli, A.K. Suri, *Int. J. Ref. Met. Hard Mater.* 35 (2012) 32–40.
- 525 [14] J. Matsushita, T. Suzuki, A. Sano, *J. Ceram. Soc. Jpn.* 101 (9) (1993)
- 526 1074–1077.
- 527 [15] B. Basu, G.B. Raju, A.K. Suri, *Int. Mater. Rev.* 51 (6) (2006) 352–
- 528 374.

- 529 [16] Z.H. Zhang, X.B. Shen, F.C. Wang, S.K. Lee, Q.B. Fan, M.S. Cao,
530 *Scr. Mater.* 66 (3–4) (2012) 167–170.
- 531 [17] C. Subramanian, T.S.R.C. Murthy, A.K. Suri, *Int. J. Refract. Met.*
532 *Hard Mater.* 25 (4) (2007) 345–350.
- 533 [18] R.G. Munro, *J. Res. Natl. Inst. Stand. Technol.* 105(2000)709-720.
- 534 [19] D.L. Ren, Q. Deng, J. Wang, J.S. Yang, Y.B. Li, J.Q. Shao, M. Li, J.
535 Zhou, S.L. Ran, S.Y. Du, Q. Huang, *J. Am. Ceram. Soc.* 101 (2018) 1–7.
- 536 [20] J.C. Wurst, J.A. Nelson, *J. Am. Ceram. Soc.* 55 (2) (1972) 109.
- 537 [21] P.A. Medwick, H.E. Fischer, R.O. Pohl, *J. All. Comp.* 203 (1994)
538 67-75.
- 539 [22] S. Yamada, K. Hirao, Y. Yamauchi, S. Kanzaki, *J. Eur. Ceram. Soc.*
540 23 (2003) 1123-1130.
- 541 [23] Y. Zhu, H.W. Cheng, Y.W. Wang, R. An, *J. All. Comp.* 772 (2019)
542 537-545.
- 543 [24] M.S. Heydari, H.R. Baharvandi, K. Dolatkhah, *Int. J. Refract. Met.*
544 *Hard Mater.* 51 (2015) 6-13.
- 545 [25] J. Cook, J. E. Gordon, C. C. Evans, D. M. Marsh, *Proc. R. Soc. Lond.*
546 A 282(1964)508-520.
- 547 [26] G.R. Anstis, P. Chantikul, B.R. Lawn, D.B. Marshall, *J. Am. Ceram.*
548 *Soc.* 64 (1981) 533-538.
- 549 [27] K. Gillet, G. Roma, J.P. Crocombette, D. Gosset, *J. Nucl. Mater.* 512
550 (2018) 288-296.

- 551 [28] V. Motte, D. Gosset, T. Sauvage, H. Lecoq, N. Moncoffre, J. Nucl.
552 Mater. 517 (2019) 165-174.
- 553 [29] A. Schneider, G. Roma, J.P. Crocombette, V. Motte, D. Gosset, J.
554 Nucl. Mater. 498 (2017) 157-162.
- 555 [30] D. Horlait, D. Gosset, A. Jankowiak, V. Motte, N. Lochet, T. Sauvage,
556 E. Gilabert, J. Nucl. Mater. 527(2019)151834.
- 557 [31] M.H. Cui, J. Wang, Z.G. Wang, T.L. Shen, K.F. Wei, C.F. Yao, J.R.
558 Sun, N. Gao, Y.B. Zhu, L.L. Pang, D. Wang, H.P. Zhu, Y. Han, X.S. Fang,
559 Nucl. Instrum. Methods Phys. Res., Sect. B 406 (2017) 611-617.
- 560 [32] Ilya A. Ovid'ko, Rev. Adv. Mater. Sci. 1 (2000) 61-107.
- 561 [33] I.J. Beyerlein, A. Caro, M.J. Demkowicz, N.A. Mara, A. Misra, B.P.
562 Uberuaga, Mater. Today 16 (2013) 443-449.
- 563 [34] D. Gosset, P. Herter, V. Motte, Nucl. Instrum. Methods Phys. Res.,
564 Sect. B 434 (2018) 66-72.
- 565 [35] P.D. Edmondson C.M. Parish, Y. Zhang, A. Hallen, M.K. Miller,
566 Scripta Mater. 65 (2011) 731-734.
- 567 [36] P. Cheminant, X. Deschanel, L. Boulanger, A. Thorel, Key Eng.
568 Mater. 132-136 (1997) 643-646.
- 569 [37] M. Carrard, D. Emin, L. Zuppiroli, Phys. Rev. B 51 (1995)
570 11270-11274.
- 571 [38] A. Bhattacharya, C.M. Parish, T. Koyanagi, C.M. Petrie, D. King, G.
572 Hilmas, W.G. Fahrenholtz, S.J. Zinkle, Y. Katoh, Acta Mater. 165 (2019)

573 26-39.

574

575 Figure captions

576 Fig. 1. Displacement damage and He concentration as a function of
577 penetration depth in B_4C and TiB_2 material, respectively.

578 Fig. 2. SEM images of surface morphology of (a) 10.5 Vol.% TiB_2
579 composites, (b) 16.2 Vol.% TiB_2 composites, and (c) 29.8 Vol.% TiB_2
580 composites; arrows indicate the TiB_2 phases.

581 Fig. 3. Geometric construction and boundary conditions of FE models: (a)
582 pure B_4C model; (b)-(d) B_4C - TiB_2 composite model based on SEM
583 image of sample S1, S2 and S3, respectively; light and dark contrasts
584 represent TiB_2 network and B_4C matrix, respectively; P_i ($i=0, 1, 2$ and 3)
585 represents middle point of the right-end boundary of each calculated
586 domain.

587 Fig. 4. Temperature distribution in pure B_4C and B_4C - TiB_2 composites
588 with different TiB_2 volume fractions at different time scales calculated by
589 FE method: (a) pure B_4C ; (b)-(d) B_4C - TiB_2 composites of sample S1, S2
590 and S3, respectively.

591 Fig. 5. Temperature variation at points P_i (center of the right-end
592 boundary in each model) with respect to time.

593 Fig. 6. Typical Vickers indentation impressions on (a) 10.5 Vol.% TiB_2
594 composites, (b) 16.2 Vol.% TiB_2 composites, and (c) 29.8 Vol.% TiB_2

595 composites. The double arrows indicate the starting to the ending of the
596 cracks.

597 Fig. 7. Statistical results of Vickers indentation-induced crack length for
598 different TiB_2 volume fractions of composites.

599 Fig. 8. SEM images of Vickers indentation-induced crack propagation;
600 solid arrows in (a) indicate deflection of cracks by isolated TiB_2 particles,
601 and dashed arrows in (b) indicate crack penetration through TiB_2 cages.

602 Fig. 9. TEM images of He bubble morphology in He deposition band in
603 B_4C phase of (a) 10.5 Vol.% TiB_2 composites, (b) 16.2 Vol.% TiB_2
604 composites, and (c) 29.8 Vol.% TiB_2 composites.

605 Fig. 10. TEM image of He bubble morphology in He deposition band and
606 at B_4C - TiB_2 interfaces. The arrows indicate the incident direction of He
607 ions. The dash lines indicate the boundaries of He bubbles band.

608

609 Table 1. Molar ratio of raw B_4C powder and Ti powder for molten-salt
610 reaction, volume fraction of TiB_2 , weight percent of TiB_2 , B_4C and C in
611 synthesized bulks.

Samples	Molar ratio ($\text{B}_4\text{C}:\text{Ti}$)	Volume fraction of TiB_2	Weight percent of TiB_2	Weight percent of B_4C	Weight percent of C
S1	6:1	10.5%	18.0%	80.4%	1.6%
S2	4:1	16.2%	26.0%	72.0%	2.0%
S3	2:1	29.8%	44.0%	52.0%	4.0%

612 Table 2. Material properties of B_4C and TiB_2 used in heat transfer

613

analysis [16, 19]

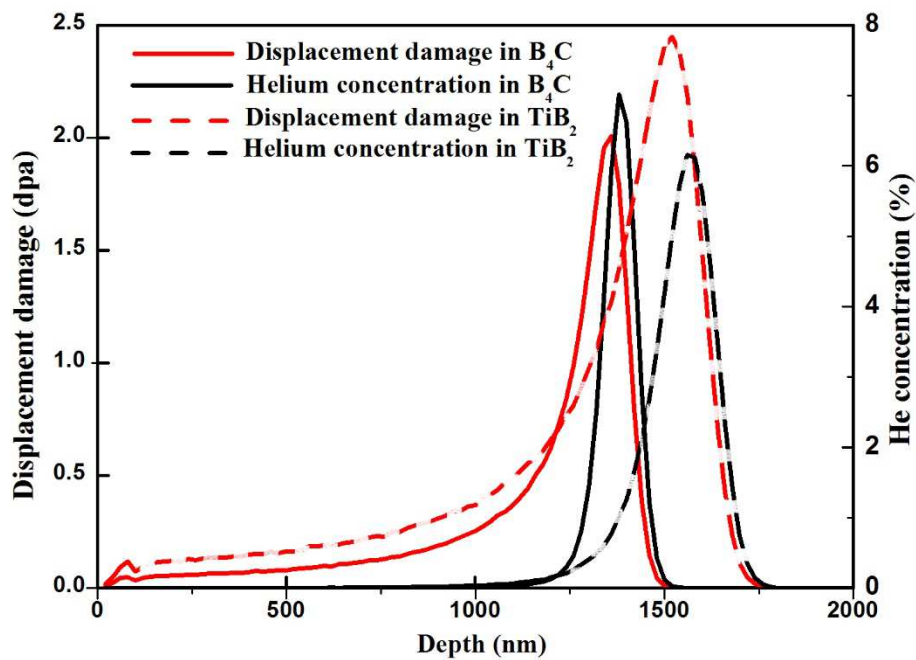
Temperature (K)	Conductivity ($\text{W}\cdot\text{m}^{-1}\cdot\text{K}^{-1}$)		Specific Heat ($\text{J}\cdot\text{kg}^{-1}\cdot\text{K}^{-1}$)		Density (kg/m^3)	
	773	1273	773	1273	773	1273
B_4C	20.00	11.00	1680.80	2072.68	2550	2550
TiB_2	81.00	78.10	1073.00	1186.00	4450	4390

614

615 Table 3. Comparison of the results calculated from real composite
 616 structure models (CM), equivalent homogeneous models (HM) and the
 617 relative error (RE).

Time (μs)	S1			S2			S3		
	CM(K)	HM(K)	RE(%)	CM(K)	HM(K)	RE(%)	CM(K)	HM(K)	RE(%)
0.2	819	836	2.1	832	856	2.9	867	901	3.9
0.4	917	948	3.4	941	981	4.3	997	1043	4.6
0.6	996	1033	3.7	1024	1069	4.4	1093	1129	4.2
0.8	1057	1093	3.7	1085	1128	4.0	1142	1180	3.3
1	1102	1137	3.2	1130	1168	3.4	1181	1212	2.6

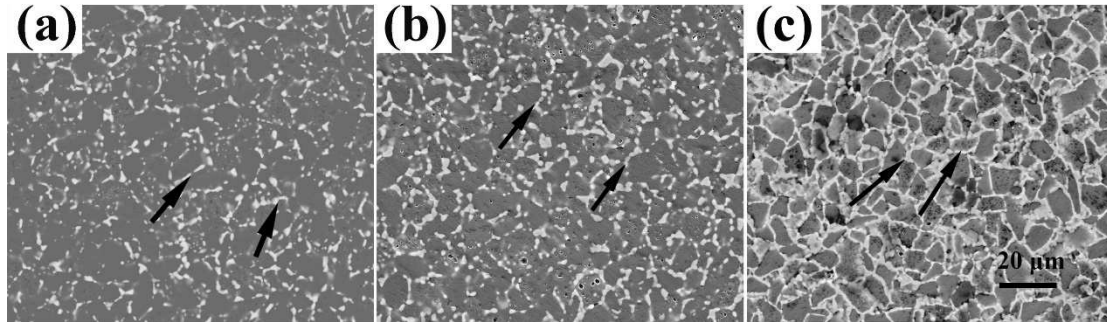
618



619

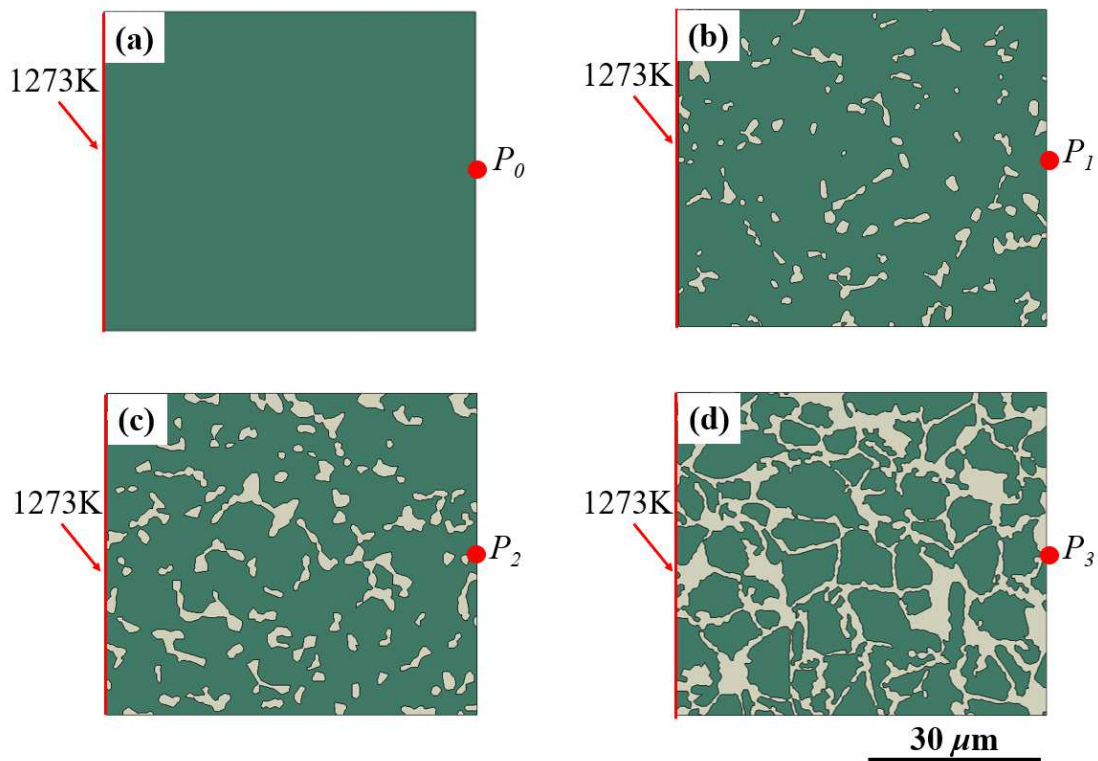
620 Fig. 1. Displacement damage and He concentration as a function of
 621 penetration depth in B_4C and TiB_2 material, respectively.

622



623

624 Fig. 2. SEM images of surface morphology of (a) 10.5 Vol.% TiB_2
 625 composites, (b) 16.2 Vol.% TiB_2 composites, and (c) 29.8 Vol.% TiB_2
 626 composites; arrows indicate the TiB_2 phases.

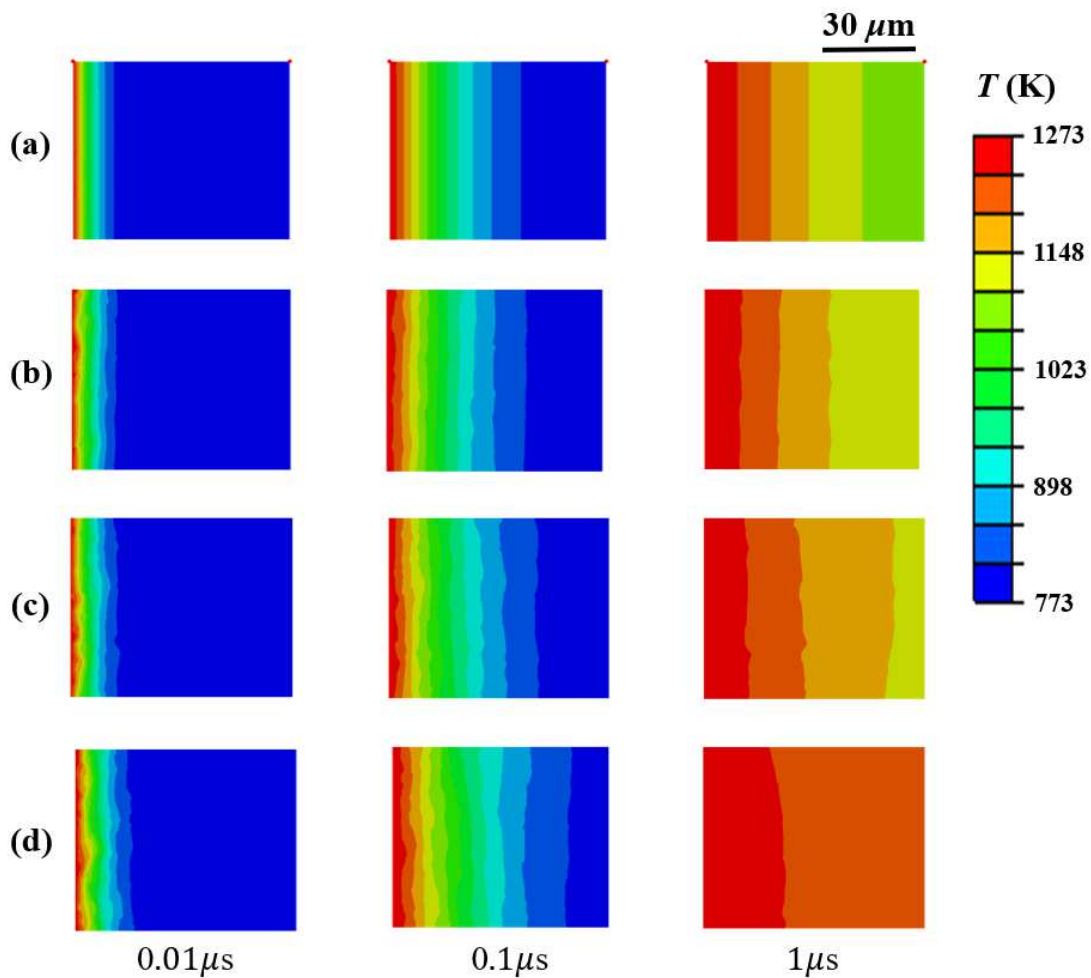


627

628 Fig. 3. Geometric construction and boundary conditions of FE models: (a)
 629 pure B_4C model; (b)-(d) B_4C - TiB_2 composite model based on SEM

630 image of sample S1, S2 and S3, respectively; light and dark contrasts
 631 represent TiB_2 network and B_4C matrix, respectively; P_i ($i=0, 1, 2$ and 3)
 632 represents middle point of the right-end boundary of each calculated
 633 domain.

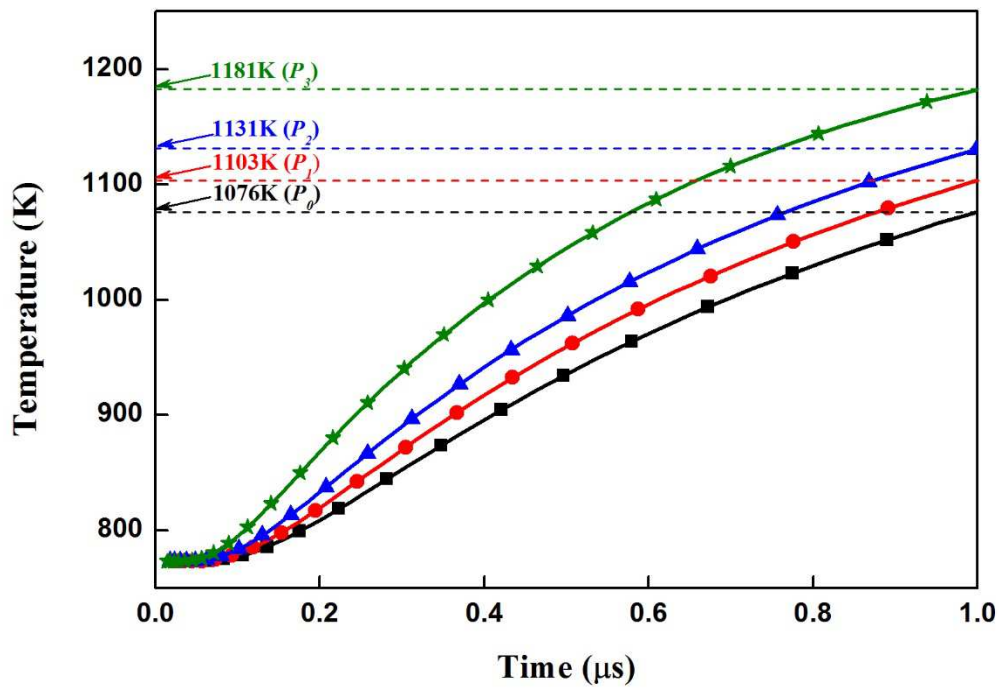
634



635

636 Fig. 4. Temperature distribution in pure B_4C and $\text{B}_4\text{C}-\text{TiB}_2$ composites
 637 with different TiB_2 volume fractions at different time scales calculated by
 638 FE method: (a) pure B_4C ; (b)-(d) $\text{B}_4\text{C}-\text{TiB}_2$ composites of sample S1, S2
 639 and S3, respectively.

640



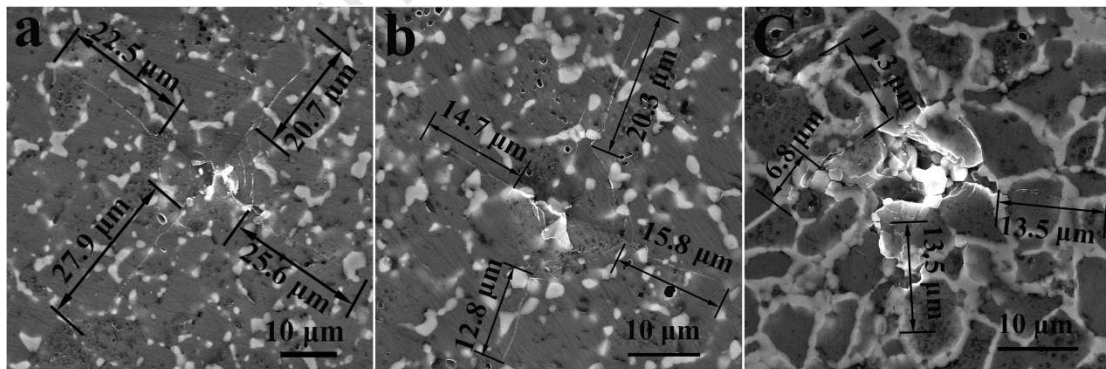
641

642 Fig.5. Temperature variation at points P_i (center of the right-end boundary

643

in each model) with respect to time.

644



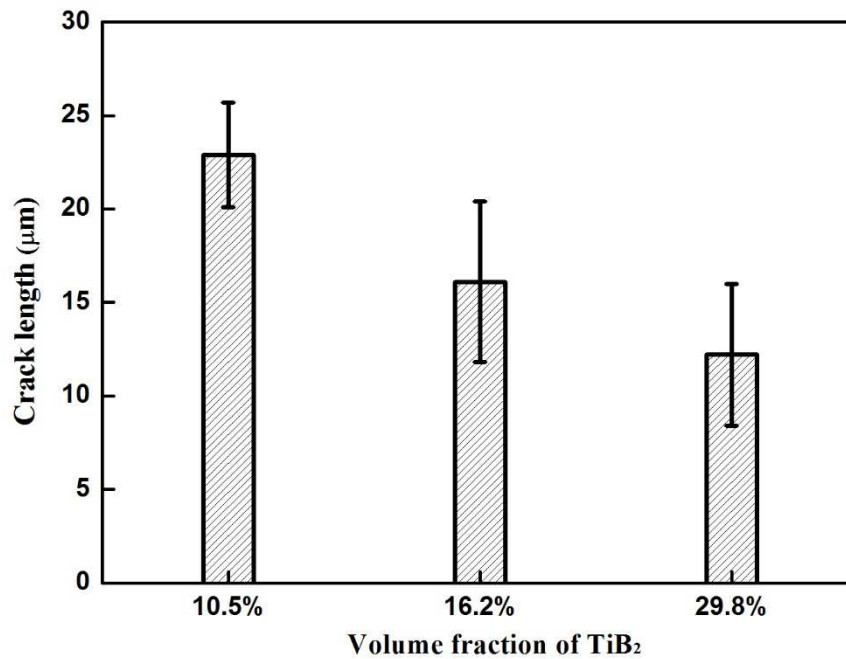
645

646 Fig. 6. Typical Vickers indentation impressions on (a) 10.5 Vol.% TiB_2 647 composites, (b) 16.2 Vol.% TiB_2 composites, and (c) 29.8 Vol.% TiB_2

648 composites. The double arrows indicate the starting to the ending of the

649

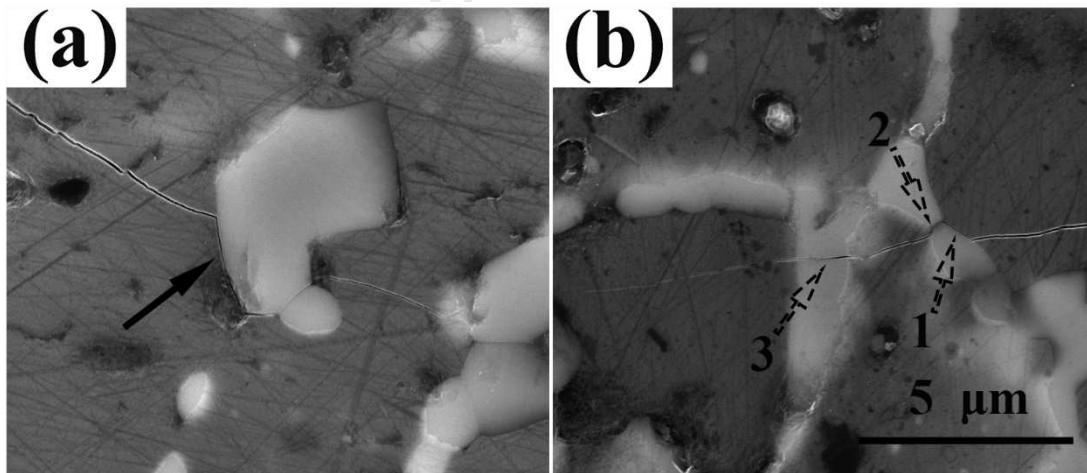
cracks.



650

651 Fig. 7. Statistical results of Vickers indentation-induced crack length for

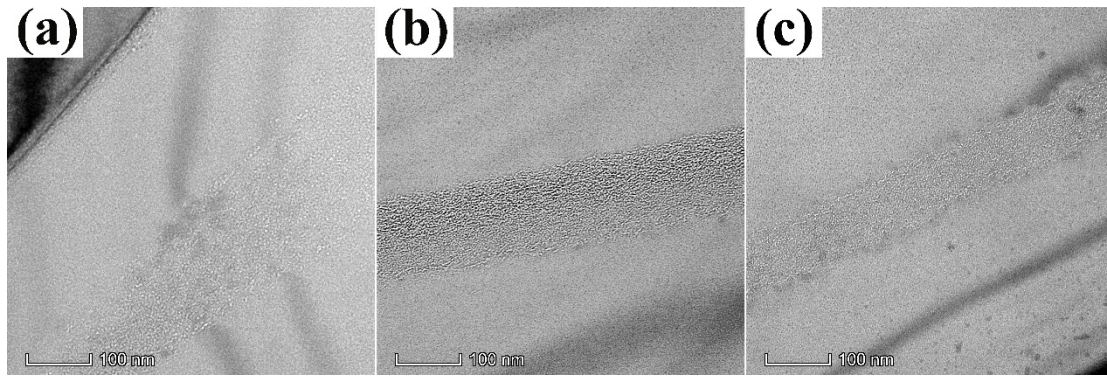
652

different TiB₂ volume fractions of composites.

653

654 Fig. 8. SEM images of Vickers indentation-induced crack propagation;

655 solid arrows in (a) indicate deflection of cracks by isolated TiB₂ particles,656 and dashed arrows in (b) indicate crack penetration through TiB₂ cages.



657

658

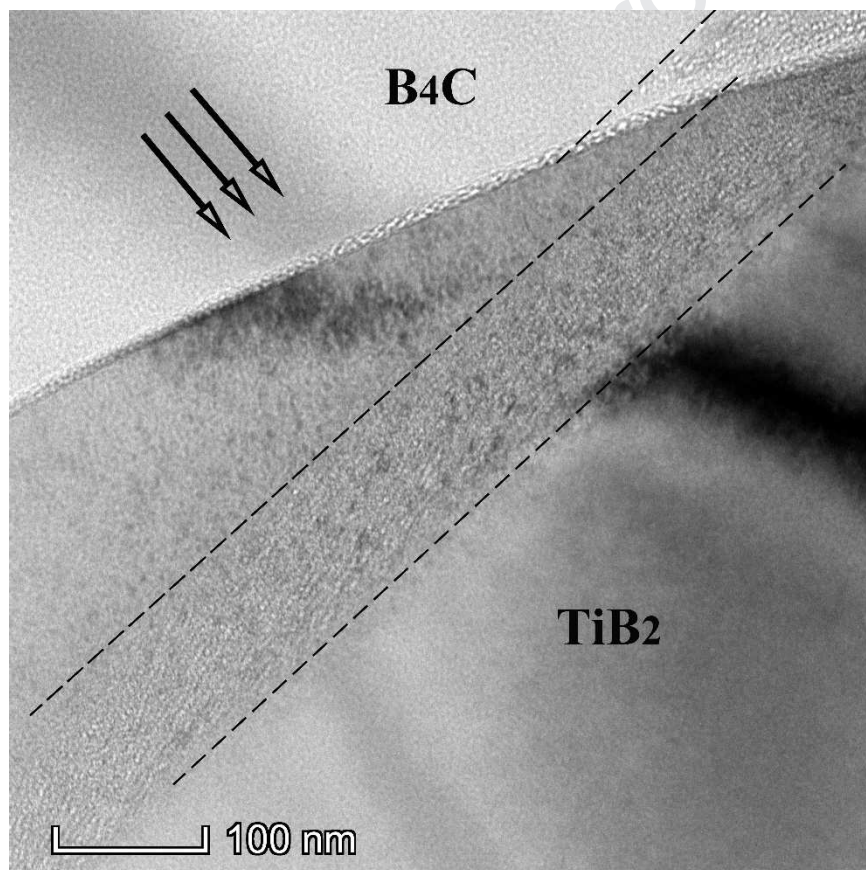
Fig. 9. TEM images of He bubble morphology in He deposition band in

659

B_4C phase of (a) 10.5 Vol.% TiB_2 composites, (b) 16.2 Vol.% TiB_2

660

composites, and (c) 29.8 Vol.% TiB_2 composites.



661

662

Fig. 10. TEM image of He bubble morphology in He deposition band and

663

at B_4C - TiB_2 interfaces. The arrows indicate the incident direction of He

664

ions. The dash lines indicate the boundaries of He bubbles band.

665

B_4C - TiB_2 composites with B_4C grains encapsulated by TiB_2 network (cages) are fabricated.

TiB_2 network (cages) greatly improve thermal conductivity and fracture toughness of B_4C - TiB_2 composites.

The interconnected interfaces between TiB_2 network (cages) and B_4C grains act as effective sinks for the aggregation of He atoms.

Declaration of interests

The authors declare that they have no known competing financial interests or personal relationships that could have appeared to influence the work reported in this paper.

The authors declare the following financial interests/personal relationships which may be considered as potential competing interests:

Journal Pre-proof